FracVAL: An improved tunable algorithm of cluster–cluster aggregation for generation of fractal structures formed by polydisperse primary particles

José Carlos Moran Cofré, A. Fuentes, Franklin Liu, Jerôme Yon

Version of Record: https://www.sciencedirect.com/science/article/pii/S0010465519300323
Manuscript_db29bcd77fb96213c7afbfc87a4663c3

FracVAL: An Improved Tunable Algorithm of Cluster-Cluster Aggregation for Generation of Fractal Structures Formed by Polydisperse Primary Particles

J. Morán[a,c,*], A. Fuentes[a], F. Liu[b], J. Yon[c]

[a] *Departamento de Industrias, Universidad Técnica Federico Santa María, Av. España 1680, Casilla 110-V, Valparaíso, Chile*
[b] *Measurement Science and Standards, National Research Council of Canada, Ottawa, Ontario, Canada*
[c] *Normandie Univ, INSA Rouen, UNIROUEN, CNRS, CORIA, 76000 Rouen, France.*

Abstract

In this study, the tunable algorithm of cluster-cluster aggregation developed by Filippov et al. 2000 for generating fractal aggregates formed by monodisperse spherical primary particles[R1.C5] is extended to polydisperse primary particles. This new algorithm, termed FracVAL[R1.C5], is developed by using an innovative aggregation strategy.[R1.C0] The algorithm is able to preserve the prescribed fractal dimension (D_f)[R1.C4] and prefactor (k_f)[R1.C4] for each aggregate, regardless of its size, with negligible error for lognormally distributed primary particles with the geometric standard deviation $\sigma_{p,geo}$ being as large as 3. In contrast, for polydisperse primary particles the direct use of Filippov et al. 2000 method, as is done by Skorupski et al. 2014, does not ensure the preservation of D_f and k_f for individual aggregates and it is necessary to generate a large number of aggregates to achieve the prescribed D_f and k_f on an ensemble basis. The performance of FracVAL is evaluated for aggregates consisting of 500 and 1000[R2.C4] monomers and for fractal dimension variation over the entire range of D_f between 1 and 3 and k_f between 0.1 and 2.7[R1.C5]. Aggregates consisting of 500 monomers[R2.C4] are generated on average in less than 2.4 minutes on a common laptop, illustrating the efficiency of the proposed algorithm.

*Corresponding author.
E-mail address: morancoj@coria.fr

Keywords: Tunable Algorithm; Fractal Aggregates; Polydisperse Primary Particles; Cluster-Cluster Aggregation

---

Program Summary

Program Title: FracVAL
Catalogue identifier:
Program summary URL:
Program obtainable from:
Licensing provisions: GNU General Public License
No. of lines in distributed program, including test data, etc.: 2,120
No. of bytes in distributed program, including test data, etc.: 139,264
Distribution format: ZIP
Programming language: Fortran 90
Computer: PC
Operating system: Windows and Linux
RAM: 1.0 Gb
Classification:
Nature of problem:
Generation of fractal-like aggregates, consisting of point-touching, polydisperse primary particles
Solution method:
Hierarchical cluster-cluster random aggregation
Additional comments including Restrictions and Unusual features:
Possible combinations of fractal dimension and prefactor depend on monomers polydispersity
Running time: Depends on the number of monomers and fractal parameters for each polydispersity level

1. Introduction

Fractal-like aggregates formed by nearly spherical primary particles are frequently encountered in many applications, such as in colloidal or aerosol systems, combustion systems, and flame synthesis of functional nanoparticles. Such particles have some remarkable and unique characteristics, e.g. large surface area and porous geometry, implying that they have high absorption capacity, good catalyst performance, fast dissolution, light-weight, and require relatively little solid material to occupy large space [1]. These particles are generated by aggregation processes which can be theoretically classified into two categories, particle-cluster [2, 3, 4, 5, 6] (PC) and cluster-cluster (CC) aggregation. A complete review of different algorithms focused on these aggregation mechanisms is found in [7]. Additionally, optimized[R1.C5] version of these algorithms can be found in more recent studies [8, 9, 10].

Under the idea of fixing the fractal dimension, Thouy and Jullien [11] introduced the first tunable CC aggregation algorithm. Subsequently, several studies are conducted to propose different tunable algorithms for fractal aggregate generation [12, 13, 14, 15, 16], though most of these studies preserved only the fractal dimension. One remarkable exception is the algorithm developed by Filippov et al. [13], which is able to preserve both the fractal dimension and the prefactor, paving the way to investigate the individual effect of D_f and k_f on the morphology and physical properties of fractal aggregates [17, 18, 19]. Some distinct features of tunable algorithms can be highlighted: (1) they allow systematic studies of the individual effects of either D_f or k_f on the physical properties of fractal aggregates; (2) a large number of aggregates can be generated numerically with a considerably low computational time; and (3) they allow the generation of fractal aggregates with prescribed D_f and k_f over a wide range irrespective of the physical aggregation mechanism.

Almost all the existing tunable algorithms developed in the literature rely on the assumption of monodisperse primary particles. One exception is the code developed by Skorupski et al. [20], which is based on the method of Filippov et al.[R1.C5] [13] and can be used to generate fractal aggregates formed by polydisperse spherical primary particles. However, the direct application of the Filippov et al.[R1.C5] [13] algorithm to generate fractal aggregates formed by polydisperse primary particles, as conducted by Skorupski et al. [20], encounters the difficulty that the resultant individual aggrgates do not preserve the prescribed fractal dimension. It is important to overcome this issue

and to develop a tunable algorithm to efficiently generate fractal aggregates formed by polydisperse primary particles, which can then be used to fill some existing gaps with regard to the effect of primary particle polydispersity on morphological properties, such as the center of mass, inertia moment, radius of gyration of sub-clusters being aggregated and consequently on the resulting structures [21, 22], as well as various physical and optical properties.

Since practical colloid or aerosol aggregates consist of polydisperse primary particles, various studies have been conducted in order to assess its influence on their morphological characterization [23, 24, 25, 21, 22], and the physical or chemical properties of such particles, such as kinetics of coagulation and sintering or coalescence, light scattering, mobility and settling [26, 27, 28, 29, 30, 31, 32, 33, 22, 34, 35]. In 2012 Eggersdorfer and Pratsinis [21] found found a dependency between aggregates morphology and monomers polydispersity.[R1.C0] Based on the above mentioned studies[R1.C0], it is important to develop efficient tunable algorithms to generate fractal aggregates formed by polydisperse PP with known D_f and k_f.

In this study, an improved hierarchical tunable algorithm of CC aggregation is developed based on the algorithm of Filippov et al. [13] to generate numerically fractal aggregates formed by polydisperse PPs.

2. Theoretical background

2.1. Primary particle size distribution

The nearly spherical primary particles constituting fractal aggregates, such as soot, fumed silica and titania, encountered in practice are always polydisperse and the primary particle size distribution (PPSD) can be commonly described by either the normal or lognormal probability density functions [36, 37]. Nevertheless, the normal distribution is not practical because for large standard deviations of the distribution it can lead to negative PP radii. Eq. (1) presents the lognormal probability density function of PP radii,

$$f[r_p] = \frac{N}{\ln[\sigma_{p,geo}]\sqrt{2\pi}r_p} \exp\left[-\frac{1}{2}\left(\frac{\ln[r_p] - \ln[r_{p,geo}]}{\ln[\sigma_{p,geo}]}\right)^2\right], \qquad (1)$$

where $f[r_p]dr_p$ is the probability of finding a particle with a radius between r_p and r_p+dr_p, $r_{p,geo}$ and $\sigma_{p,geo}$ correspond to the geometric mean and geometric standard deviation, respectively. Please note that for a population of N monomers these values are given by the following equations,[R2.C1]

$$\log(r_{p,geo}) = \frac{\sum_{i=1}^{N} \log(r_i)}{N} \tag{2a}$$

$$\log(\sigma_{p,geo}) = \sqrt{\frac{\sum_{i=1}^{N} (\log(r_i) - \log(r_{p,geo}))^2}{N}} \tag{2b}$$

It can be checked that for monodisperse primary particles the RHS of Eq. (2b) becomes zero and therefore $\sigma_{p,geo} = 1$.[R2.C1] Although the level of PP polydispersity is often fairly low with $\sigma_{p,geo} \leq 1.3$, highly polydisperse primary particles can be encountered. For example, for flame generated soot aggregates, the geometric standard derivation $\sigma_{p,geo}$ can be as high as $\sigma_{p,geo} = 2.1$ [36, 37, 38, 39], depending on the residence time, fuel type, and flame conditions.

2.2. Characterization of fractal aggregates

The mass of a fractal aggregate (m_a) follows the fractal scaling law. For an aggregate consisting of point-touch polydisperse spherical PPs [21],

$$\frac{m_a}{\overline{m_p}} = k_f \left(\frac{R_g}{r_{p,geo}} \right)^{D_f}, \tag{3}$$

where $\overline{m_p}$ is the average PP mass, i.e., $m_a/\overline{m_p} = N$, is the number of PP in the aggregate. The exponent D_f and the proportionality constant k_f in Eq. (3) are the fractal dimension and prefactor, respectively. For fractal aggregates consisting of monodisperse monomers ($\sigma_{p,geo} = 1$) generated through diffusion-limited cluster aggregation (DLCA), it has been well established that $D_f \approx 1.78$ and $k_f \approx 1.40$ [7, 40]. However, Eggersdorfer and Pratsinis [21] showed a dependency of both D_f and k_f on PP polydispersity. In fact, for aggregates formed in the same molecular regime they found that both D_f and k_f decrease with increasing PP polydispersity. They obtained $D_f = 1.68$ and $k_f = 0.98$ for $\sigma_{p,geo} = 2.0$, and $D_f = 1.48$ and $k_f = 0.77$ for $\sigma_{p,geo} = 3.0$. The ranges of these parameters are used for the generation and analysis of fractal aggregates of the present work. Finally, R_g is the radius of gyration of the aggregate calculated using the expression proposed by [22],

$$R_g^2 = \frac{1}{m_a} \sum_{i=1}^{N} m_{p,i} \left[(R_i - R_c)^2 + r_{g,i}^2 \right], \tag{4}$$

where $r_{p,i}$ and $m_{p,i}$ are respectively the PP radius and mass of the ith spherical primary particle, which is located at a distance R_i from the origin of a fixed coordinate system. The term $r_{g,i}$ is the radius of gyration of the ith PP, i.e., $r_{g,i}^2 = (3/5)r_{p,i}^2$. R_c is the center of mass of the aggregate evaluated as,

$$R_c = \frac{1}{m_a} \sum_{i=1}^{N} m_{p,i} R_i. \tag{5}$$

It can be easily shown that Eqs. (4) and (5) degrade to those for monodisperse primary particles given in Filippov et al. [13] when all the primary particles have the same mass.

3. Formulation of the improved tunable algorithm

3.1. Main equations

Consider two clusters (aggregates) with mass m_1 and m_2 and radius of gyration R_{g1} and R_{g2}, which have the same prescribed D_f and k_f and are to be aggregated to form a larger aggregate with mass $m = m_1 + m_2$ and radius of gyration R_g and to preserve both D_f and k_f. To this end, it can be shown that the distance between the mass centers of the two clusters Γ satisfies the following equation,

$$m^2 R_g^2 = m \left(m_1 R_{g1}^2 + m_2 R_{g2}^2 \right) + \Gamma^2 m_1 m_2, \tag{6}$$

The consequence and advantage of using Eq. (6), as it will be demonstrated later, are that it ensures the preservation of both D_f and k_f[R1.C5] during each step of the aggregation process for each individual aggregate generated. The derivation of this equation is provided in Appendix A. In the special case of two aggregates consisting of N_1 and N_2 monodisperse PPs ($N = N_1 + N_2$), Eq. (6) is reduced to,

$$N^2 R_g^2 = N \left(N_1 R_{g1}^2 + N_2 R_{g2}^2 \right) + \Gamma^2 N_1 N_2, \tag{7}$$

which is identical to the relationship derived by Filippov et al. [13], i.e., the derived Eq. (6) is the generalized form of Eq. (7) for aggregates consisting of polydisperse PPs. Eq. (6) represents an original contribution of the present study and forms one of the main relations of the present tunable algorithm.

3.2. FracVAL: A tunable cluster-cluster aggregation algorithm

The FracVAL (fractal aggregate generation algorithm developed in Valparaíso) algorithm is programmed in a hierarchical manner, i.e., only aggregation between sub-clusters with approximately the same number of primary particles is allowed [11]. The algorithm consists of four main steps corresponding to the flow chart shown in Fig. 6 and it is described as follows.

Step 1: The fractal dimension D_f (between 1 and 3) and the fractal prefactor k_f (a positive value, typically on the order of unity) of aggregates to be generated are prescribed, which will be preserved during the entire fractal aggregate generation process. In addition, the primary particle radius distribution and the aggregate size N (the number of primary particles contained in the aggregate) are also required. The PPSD is assumed lognormal and characterized by the geometric mean and standard standard deviation, i.e., $r_{p,geo}$ and $\sigma_{p,geo}$. To obtain a total of N radii from this lognormal distribution given by Eq. (1), a pseudo-random number generator is used [41]. To avoid extremely large and extremely small values of PP radius, which are unrealistic, the selection of PP radii is constrained to the following range $[r_{p,geo}/\sigma^2_{p,geo}, r_{p,geo}\sigma^2_{p,geo}]$, which contains 95.5% of the radii.

Step 2: A particle-cluster aggregation algorithm is first used to obtain a total of I_t sub-clusters (smaller aggregates) consisting of approximately the same number of primary particles (N_{sub}), where $\sum_{I_t} N_{sub} = N$. This criterion is introduced in order to mimic the hierarchical aggregation of particles that possess the self-similarity of fractal aggregates [42]. In the present work N_{sub} is selected depending on N. For N$\in$[50,500], each sub-cluster[R1.C5] consists of $N_{sub} = 0.1N$ and under the lower limit (N$\leq$ 50) a constant $N_{sub} = 5$ is employed. On the other hand, above the upper limit (N$\geq$ 500) a constant $N_{sub} = 50$ is[R1.C5] used. This type of particle-cluster aggregation algorithms has been found to experience some difficulties for retaining exactly the fractal parameters and therefore small N_{sub} are recommended in the literature in order to avoid effects in the final aggregates [13, 20]. In this context, a sensitivity analysis is included in the Appendix C. The main conclusion of this analysis is that for $N_{sub} < 0.15N$ there is not effect on the morphology of final aggregates. Additionally, an variation of $\pm$20% of D_f or k_f for the initial sub-clusters is expected to have a relatively small effect on the density-density correlation function of the final aggregates.[R1.C4]

Step 3: In this step, the sub-clusters generated in Step 2 are organized into pairs that are able to aggregate to form a larger cluster. This "ability to aggregate" is defined according to the criterion $R_{max,1} + R_{max,2} \geq \Gamma_{12}$, where

$R_{max,i}$ corresponds to the furthest distance of a PP to the center of mass of the ith aggregate (i = 1,2) and Γ_{12} is the distance between the centers of mass of the two sub-clusters to be aggregated and calculated as,

$$\Gamma_{12} = \frac{1}{\sqrt{m_1 m_2}} \left[m^2 R_g^2 - m \left(m_1 R_{g1}^2 + m_2 R_{g2}^2 \right) \right]^{1/2}, \tag{8}$$

where m_1, m_2, R_{g1} and R_{g2} are the masses and radii of gyration of the two sub-clusters being aggregated. Additionally, $m = m_1 + m_2$ and R_g are the corresponding parameters for the resulting larger aggregate. The radii of gyration R_{g1}, R_{g2} and R_g are calculated from the scaling law,

$$R_{gi} = r_{p,geo} \left(\frac{n_i}{k_f} \right)^{1/D_f} \tag{9}$$

where n_i is the number of monomers of the ith aggregate (here for both the sub-clusters and the resultant larger aggregate) and D_f and k_f are the prescribed fractal parameters.

Step 4: This is the main part of the algorithm. In this step, the two sub-clusters belonging to the same pair determined in Step 3 are aggregated to form a larger aggregate. It is based on the idea that there are two sub-clusters, from here onwards they will be called sub-cluster A1 (containing N_1 monomers) and sub-cluster A2 (containing N_2 monomers), that can be aggregated in many different ways, each of these ways associates a distance between the center of mass of aggregates A1 and A2, but there is only one distance (represented by Γ_{12} in Eq. (8)) that ensures the preservation of both D_f and k_f. Therefore, knowing this distance, our goal only consists in finding one of the possible paths to combine the clusters by keeping the distance between them fixed.[R2.C3] To better describe this step, it is divided into 6 sub-steps as shown in Fig. 6.

- **Sub-step a**: Select a pair of sub-clusters A1 and A2[R2.C3] from the pairs determined in Step 3.

- **Sub-step b**: Create a binary matrix a_{ij}. Let d_{i1} and d_{j2} be respectively the distance from the center of monomer i (in A1, i = 1,2,...,N_1) and j (in A2, j = 1, 2,..., N_2) to the center of mass of A1 and A2, respectively. Assign $a_{ij} = 1$ when:

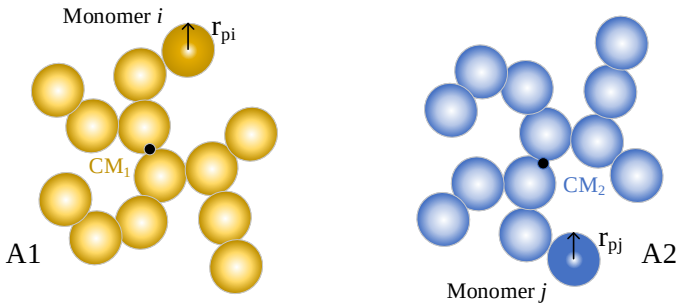

Figure 1: Sub-clusters A1 and A2 selected to be aggregated.

The restriction defined by Eq. (10) is fulfilled, this restriction ensures that both monomers are close enough to be in point-touching,

$$D_{i1,+} + D_{j2,+} \geq \Gamma_{12}, \tag{10}$$

where $D_{i1,+} = d_{i1} + r_{pi}$, $D_{i1,-} = d_{i1} - r_{pi}$, $D_{j2,+} = d_{j2} + r_{pj}$ and $D_{j2,-} = d_{j2} - r_{pj}$. Additionally, there is a lower limit defined by 3 possible cases described as follows,

- Case 1: When the spheres of radius $D_{i1,+}$ and $D_{j2,+}$ can be intersected (see Fig. 2), this means that $|D_{i1,+} - D_{j2,+}| \leq \Gamma_{12}$.

  The two following cases are associated with the intersection of the spheres with radius $D_{i1,-}$ and $D_{j2,-}$.

- Case 2: When the sphere of radius $D_{i1,+}$ is too big containing the sphere of radius $D_{j2,+}$, i.e. when $(D_{i1,+} - D_{j2,+}) > \Gamma_{12}$ with an[R1.C5] upper limit $D_{i1,-} \leq \Gamma_{12} + D_{j2,+}$.

- Case 3: Analogously, when the sphere of radius $D_{j2,+}$ is too big containing the sphere of radius $D_{i1,+}$, i.e. when $(D_{j2,+} - D_{i1,+}) > \Gamma_{12}$ with an upper limit $D_{j2,-} \leq \Gamma_{12} + D_{i1,+}$.

Please note that Case 2 and Case 3 are theoretically and mathematically possible, and they are considered in FracVAL. Please see the Appendix D for a further explanation of Cases 2 and 3.[R1.C1] However,

Case 1 is considered the most common one, and therefore it is used to explain the subsequent steps of the algorithm.

These restrictions ensure that ith monomer belonging to A1 is able to aggregate with the jth monomer belonging to A2; otherwise, assign $a_{ij} = 0$. For the pair A1 and A2, Γ_{12} is evaluated using Eq. (8).

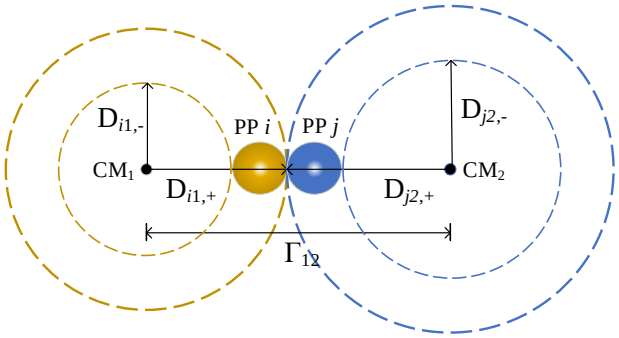

Figure 2: Example of intersection between the spheres of radius $D_{i1,+}$ and $D_{j2,+}$ can be intersected.

- **Sub-step c**: Loop over the elements of the binary matrix a_{ij}. If $a_{ij} = 0$, continue the loop. If $a_{ij} = 1$, assign the ith primary particle in A1 as s1 and the the jth primary particle in A2 as s2.

The goal of Step 4 is to aggregate the sub-clusters A1 and A2. Specifically, the algorithm needs to find the locations of the mass centers of A1 and A2 and the proper orientations of A1 and A2 upon aggregation to satisfy the following restrictions:
First, the distance between the centers of mass of A1 and A2 is Γ_{12} given by[R1.C5] Eq. (8). Secondly, the selected primary particle candidates s1 (belonging to A1) and s2 (belonging to A2) are in point-touch. Thirdly, there is no overlapping between any primary particles in A1 and A2. The above mentioned 3 restriction will be satisfied progressively by 3 stages described as follows,[R1.C2]

  - **Stage 1:** To satisfy restriction 1 we retain the center of mass of A1 (referenced as CM1 = $(X_{cm,1}, Y_{cm,1}, Z_{cm,1})$) fixed while the center

of mass of A2 (referenced as CM2 = $(X_{cm,2}, Y_{cm,2}, Z_{cm,2})$) is placed at a distance Γ_{12} from CM1. This displacement is made along the unitary direction defined by CM1 and the center of s1. At this point we already fulfil restriction 1. This is shown in Fig. 3.[R1.C2]

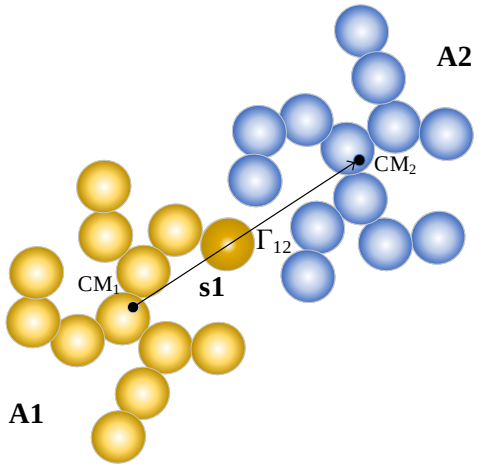

Figure 3: Displacement of A2 to fulfill restriction (1).

– **Stage 2:** Next, we will rotate A1 and A2 in the following manner to fulfill restrictions 2 and 3. Firstly, A1 is rotated, to this end we calculate the distances d_{s1} and d_{s2} from monomers s1 and s2 to CM1 and CM2, respectively, and place the monomer s1 at a tangential point defined by the interception of two of the following spheres as illustrated in Fig. 4.[R1.C2]

$$D^2_{s1,+} = (X - X_{cm,1})^2 + (Y - Y_{cm,1})^2 + (Z - Z_{cm,1})^2, \quad (11a)$$

$$D^2_{s2,+} = (X - X_{cm,2})^2 + (Y - Y_{cm,2})^2 + (Z - Z_{cm,2})^2, \quad (11b)$$

This random point can be determined analytically by considering the following procedure (Here the reader may go directly to Stage 3 without loss of continuity). As shown in Fig. 5, the sphere-sphere

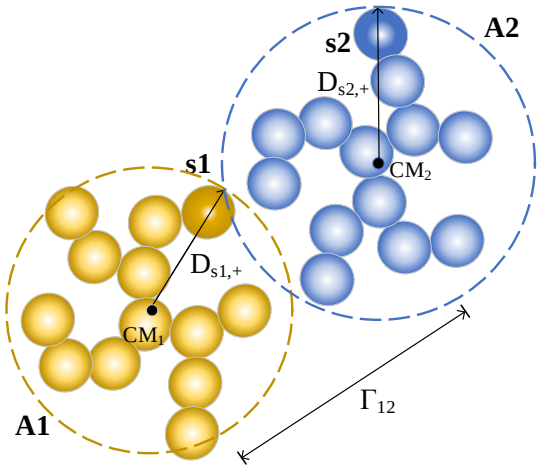

Figure 4: Location of monomer s1 given by the intersection of spheres given by Eq. (11a) and Eq. (11b).

intersection corresponds to a circle that can be parametrized by the equation (12),[R1.C2]

$$\vec{r}[\psi] = \vec{c} + \rho\cos[\psi]\hat{i}' + \rho\sin[\psi]\hat{j}', \qquad \psi \in [0, 2\pi] \qquad (12)$$

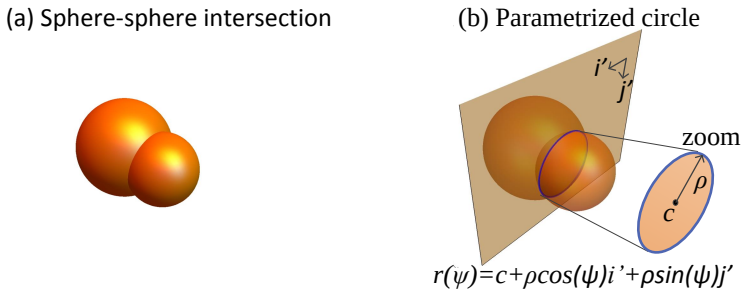

Figure 5: Sphere-sphere intersection and circle parametrization.

where $\vec{c}$ and ρ are the coordinates of the geometric center and the radius of this circle, respectively. Additionally, $\hat{i}'$ and $\hat{j}'$ are

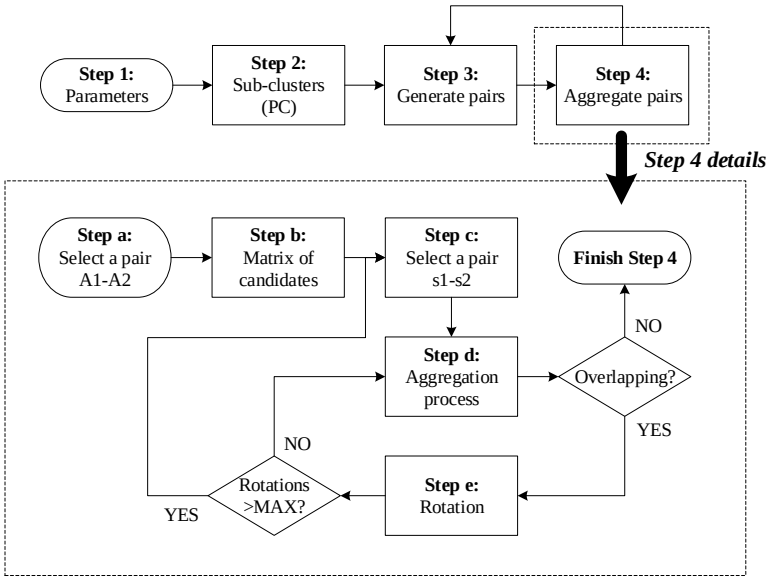

Figure 6: Flow chart of FracVAL cluster cluster aggregation algorithm.

unit vectors perpendicular between them and belonging to the plane where the circle is embedded. All of this parameters can be determined analytically as explained in Appendix B. Finally, the vector $\vec{r}[\psi]$ brings[R1.C5] the coordinates of a point belonging to this circle with orientation ψ. Therefore, the work of this step is reduced to just find a random angle $\psi \in [0, 2\pi]$. Subsequently, the orientation of each other PP belonging to A1 is updated based in the rotation of s1 by using the Euler-Rodriguez model [43].

– **Stage 3:** The location of s2 is determined by finding a random point in the interception of the two spheres,[R1.C2]

$$(r_{s1} + r_{s2})^2 = (X - X_{s1})^2 + (Y - Y_{s1})^2 + (Z - Z_{s1})^2, \qquad (13a)$$

$$d_{s2}^2 = (X - X_{cm,2})^2 + (Y - Y_{cm,2})^2 + (Z - Z_{cm,2})^2, \qquad (13b)$$

where Eq. (13a) ensures that both candidates s1 and s2 will be in one point touch and Eq. (13b) ensures that candidate s2 will retain their relative distance to the center of mass of aggregate

A2 and therefore restrictions 1 and 2 mentioned above will be fulfilled. This is illustrated in Fig. 7.[R1.C2] One point in the in-

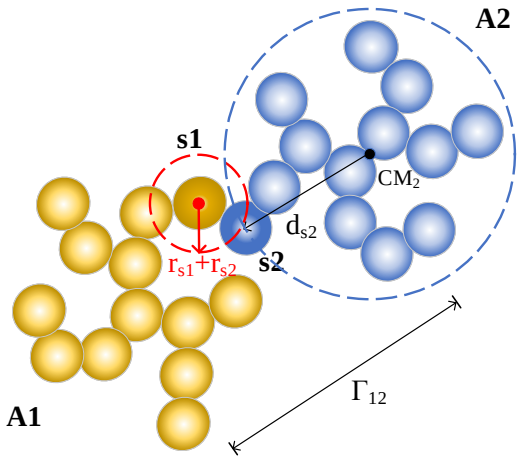

Figure 7: Intersection of spheres given by Eq. (13a) and Eq. (13b).

tersection of these two spheres is found using the same procedure described by equation (12). Subsequently the whole aggregate A2 is rotated based in the rotation of s2 by using the Euler-Rodriguez model [43]. At this point, restrictions 1 and 2 are ensured. Restriction 3 is not necessarily ensured, so the algorithms continue with sub-step d to check it.[R1.C2]

- **Sub-step d**: Eventually, in the current orientation of A1 and A2 overlapping between PP exists. In this case the orientation of A2 is modified by random rotation by using the Euler-Rodriguez formula [43] and using the solution of the intersection of spheres given by Eq. (13a) and Eq. (13b), i.e. monomer s2 is rotated around monomer s1.

  In case that overlapping still exists (following a maximum number of iteration defined by the user), the algorithm return to sub-step c and it picks another pair of monomers s1 and s2. Finally at this point, restrictions 1, 2 and 3 are ensured.

4. Validation

4.1. Primary particle size distribution

Figure 8 shows the histogram of primary particle radii for an aggregate consisting of $N = 1024$ primary particles sampled from a lognormal distribution with $\sigma_{p,geo} = 2.0$ and $r_{p,geo} = 15.0$ nm. It is evident that the specified PPSD iss well preserved. When the Kolmogorov-Smirnov goodness-of-fit test (D) is applied, a value of $D = 0.03$ is obtained. A significance of $\alpha = 0.01$ corresponds to a critical value of $C_{\alpha=0.01} = 0.05$. Since $D < C_{\alpha=0.01}$, the radius of the primary particles of the aggregate effectively satisfies the specified lognormal size distribution.

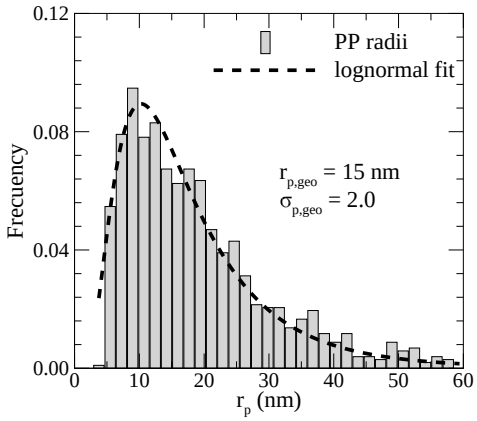

Figure 8: Histogram of radii of primary paticles in an aggregate of $N = 1024$ sampled from a lognormal PPSD with $\sigma_{p,geo} = 2.0$ and $r_{p,geo} = 15.0$ nm showing the preservation of the specified distribution.

4.2. Density-density correlation function

It is expected that the spatial distribution of the mass of an aggregate should follow a specific behavior to be considered as fractal [44]. The density-density correlation function is usually examined to test if the generated aggregates possess the expected fractal behavior in addition to the scaling law [45, 13]. For the particular case of aggregates formed by[R2.C5] polydisperse primary particles, Bushell and Amal [24] suggested to use the partial distance distribution function, which unfortunately is not practical when dealing with lognormally distributed primary particles, this because

there are too many different radii to obtain a partial distribution function as proposed in the mentioned reference. Therefore, we developed a new alternative to evaluate it. Let $f(r)$ be the density-density correlation function evaluated at a distance r from the mass center of the aggregate. This value is calculated in an iterative manner for radius in the range $r \in [R_{min}, R_{max}]$, where $R_{min} = r_{p,geo}/10$ and $R_{max} = \delta R_g$, i.e., δ times the radius of gyration of the aggregate. Normally, a value of $\delta = 3.5$ is considered sufficiently large. At the kth iteration, radius r is discretized as follows,

$$r^{(k)} = R_{min}(R_{max}/R_{min})^{k/(n_{it}-1)}. \tag{14}$$

where $k \in [1, (n_{it}-1)]$, with n_{it} being a total number of discretized radii considered. For a given k, a "copy" of the aggregate is generated and displaced at a distance $r^{(k)}$ from the mass center of the original aggregate in a random direction (i.e., a random point in a sphere). Then the volume of intersection of both aggregates $V_{int}^{(k)}$ is analytically determined based on the concept of spherical cap [46]. Hence, this process is repeated until a total of n_{or} orientations is evaluated. Finally, the density-density correlation function is calculated by averaging the volumes of intersection over all orientations and dividing by the total volume of the aggregate V_a,

$$f(r^{(k)}) = \frac{\frac{1}{n_{or}} \sum_{n_{or}} V_{int}^{(k)}}{V_a}, \tag{15}$$

4.2.1. Aggregates formed by monodisperse PP

In Fig. 9 samples of the generated aggregates consisting of monodisperse primary particles are shown. These aggregates are generated for three different fractal dimensions of $D_f = 1.40$, 1.79, and 2.40 and four aggregate sizes of $N = 20$, 50, 500, and 1024. It is evident that a larger fractal dimension leads to a more compact structure. As a way to validate our algorithm, the density-density correlation function $f(r)$ is calculated as described above considering a total of $n_{or} = 300$ orientations for each case.

The calculated density-density correlation functions $f(r)$ for different aggregate sizes from $N = 20$ up to $N = 1024$ generated using FracVAL[R1.C5] and using the algorithm developed by Skorupski et al. [20] are compared in Fig. 10. It is noticed that these aggregates are generated from monodisperse primary particles.

The density-density correlation function $f(r)$ corresponds to the spatial mass distribution of the aggregate, and it is supposed to exhibit a slope of

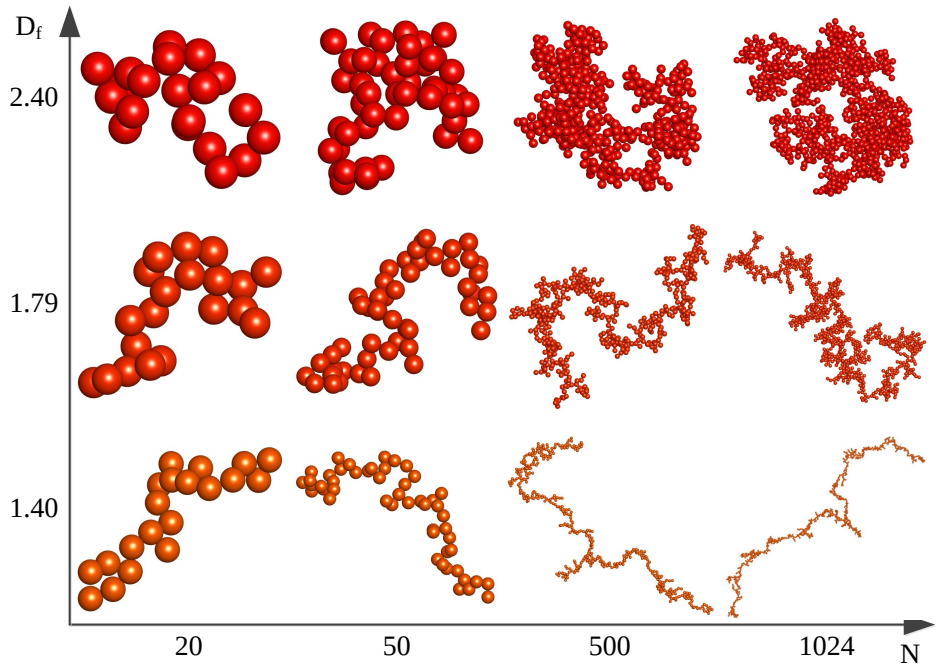

Figure 9: Selected aggregates generated by FracVAL with monodisperse PP ($\sigma_{p,geo} = 1.0$) for $D_f = 2.40$, $k_f = 0.80$ (top row), $D_f = 1.79$, $k_f = 1.40$ (middle row), and $D_f = 1.40$, $k_f = 1.80$ (bottom row).

$D_f - d$, where d is the Euclidean dimension of space ($d = 3$), for sufficiently large aggregates. However, due to the natural cut-off of fractal aggregates of finite size this behavior can be expected only in a limited range of r [44]. As can be seen in Fig. 10, the agreement in $f(r)$ for aggregates generated from both algorithms is very good, especially for large N. In addition, the expected slope of the decay of $f(r)$ with r for sufficiently large N, i.e., $D_f - d$, is progressively displayed with increasing N, consistent with the findings of Filippov et al.[R1.C5] [13]. As can be noted, the agreement of calculated $f(r)$ with the theoretical behaviour is progressively better for larger aggregates, this is explained by the finite size effects on $f(r)$, which imply that smaller aggregates, namely $N = 20$, the $f(r)$ function is predominated by the cut-off function.[R1.C5]

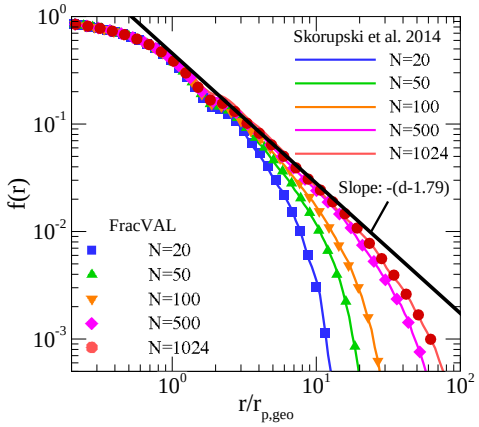

Figure 10: The density-density correlation functions of aggregates formed by monodisperse primary particles with $D_f = 1.79$, $k_f = 1.40$. The solid lines correspond to the aggregates generated by using[R1.C5] the algorithm of Skorupski et al. 2014 and symbols are for aggregates generated by[R1.C5] using FracVAL. d stands for the Euclidean dimension of space $d = 3$.

4.2.2. Aggregates formed by polydisperse primary particles

In Fig. 11 samples of aggregates formed by lognormally distributed polydisperse primary particles with $\sigma_{p,geo} = 2.0$ using FracVAL[R1.C5] are shown. These aggregates are generated for $D_f = 2.60$, $k_f = 0.25$ (top row)[R1.C5], $D_f = 1.68$, $k_f = 0.98$ (middle row), and $D_f = 1.30$, $k_f = 1.50$[R1.C5] (bottom row) and for four aggregate sizes of $N = 20$, 50, 500 and 1024.

Fig. 12(a) and Fig. 12(b) show the density-density correlation function of fractal aggregates of $N = 100$ and 1024, respectively, generated using FracVAL for polydispersity levels ranging from $\sigma_{p,geo} = 1.0$ (monodisperse) to $\sigma_{p,geo} = 3.0$ (extremely polydisperse) and for different fractal properties as shown in the figure legend. As can be seen, the expected power law behavior becomes more evident, i.e., the linear decay of $f(r)$ with r in the log-log scale plot, especially for $N = 1024$. It is interesting to notice that the power law behavior seems to extend over a larger range of r for $\sigma_{p,geo} = 2$. Moreover, the slope of the calculated density-density correlation function is in good agreement with the theoretical slope of $(D_f - d)$ for all the three combinations of D_f and $\sigma_{p,geo}$, i.e., $D_f = 1.79$ and $\sigma_{p,geo} = 1.0$, $D_f = 1.68$ and $\sigma_{p,geo} = 2.0$, and $D_f = 1.48$ for $\sigma_{p,geo} = 3.0$. These values of D_f correspond to those of DLCA aggregates when considering different levels of primary particle

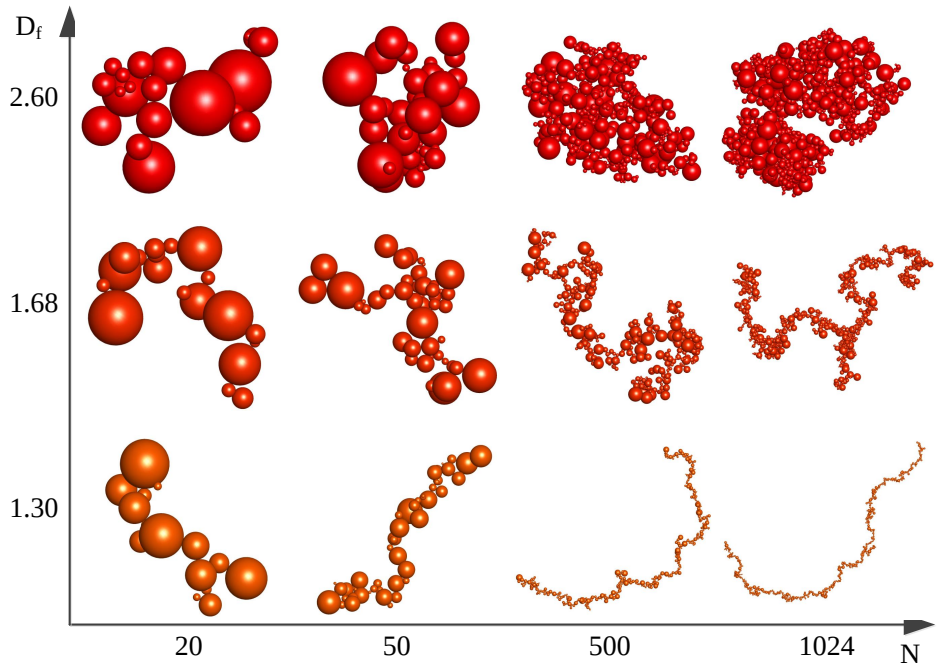

Figure 11: Sample aggregates generated by FracVAL from polydisperse PPs[R1.C5] with $\sigma_{p,geo} = 2.0$ and specified fractal parameters of $D_f = 2.60$, $k_f = 0.25$ (top row), $D_f = 1.68$, $k_f = 0.98$ (middle row), and $D_f = 1.30$, $k_f = 1.50$ (bottom row)[R1.C5].

polydispersity [21]. As expected, the agreement is better for $N = 1024$ rather than $N = 100$, consistent with the results shown for monodisperse primary particles in Fig. 10.

4.3. Preservation of prescribed fractal parameters

An important feature of tunable algorithms is to ensure each individual aggregate generated accurately satisfies the scaling law expressed in Eq. (9), regardless of its size. Specifically, each individual aggregate generated by a tunable algorithm possesses the same D_f and k_f as the prescribed values. This requirement is naturally built into the algorithm through the application of Eq. (9) during the generation.

To probe the preservation of fractal parameters (D_f and k_f) on a global sense, i.e., to examine an ensemble of aggregates of different sizes, plots of $\log(N) - \log(R_g/r_{p,geo})$ for different prescribed fractal dimension and pref-

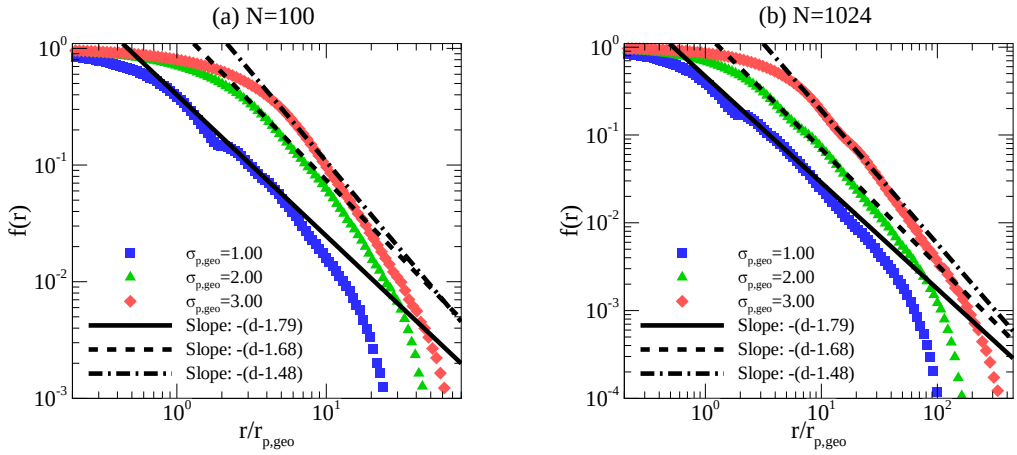

Figure 12: The calculated density-density correlation functions of aggregates consisting of $N = 100$, $N = 1024$ primary particles of different levels of polydispersity. The imposed fractal parameters are: $D_f = 1.79$, $k_f = 1.40$ for $\sigma_{p,geo} = 1.0$, $D_f = 1.68$, $k_f = 0.98$ for $\sigma_{p,geo} = 2.0$, and $D_f = 1.48$, $k_f = 0.77$ for $\sigma_{p,geo} = 3.0$. d stands for the Euclidean dimension of space with $d = 3$.

actor are presented in Fig. 13(a) and 13(b) for monodisperse ($\sigma_{p,geo} = 1$) and polydisperse ($\sigma_{p,geo} = 2$) primary particles, respectively. The aggregate size is varied non-uniformly from $N = 20$ to 1024. It is important to note that each data point in Fig. 13 corresponds to 50 aggregates. As observed in the figure, each condition for individual aggregates (characterized by D_f, k_f, N, and $\sigma_{p,geo}$) accurately preserves the prescribed fractal parameters. The solid lines represent the log-log fit of the data points and the corresponding parameters are reported in the figure legend. It is evident that all the curves display a linear variation of N with the normalized R_g in the log-log plot expected from the scaling law of Eq. (3).

As can be seen in Fig. 13(a) for all thee three sets of aggregates formed by monodisperse primary particles, the fractal scaling law is very accurately preserved and the fractal dimension based on the slope of the linear fit deviates from the prescribed value by less than only 1%. The same observations can be made for aggregates formed polydisperse primary particles as shown in Fig. 13(b). It is worth pointing out that these pairs of D_f and k_f are selected to represent the most extreme values under which FracVAL is able to generate the fractal aggregates for the evaluated PP polydispersity ($\sigma_{p,geo} = 2$). The results shown in Fig. 13 confirm that the ensemble of aggregates gener-

ated by FracVAL strictly preserves the prescribed fractal parameters under different conditions in terms of fractal parameters (D_f and k_f) and the level of primary particle polydispersity as long as the fractal aggregates can be generated by FracVAL.

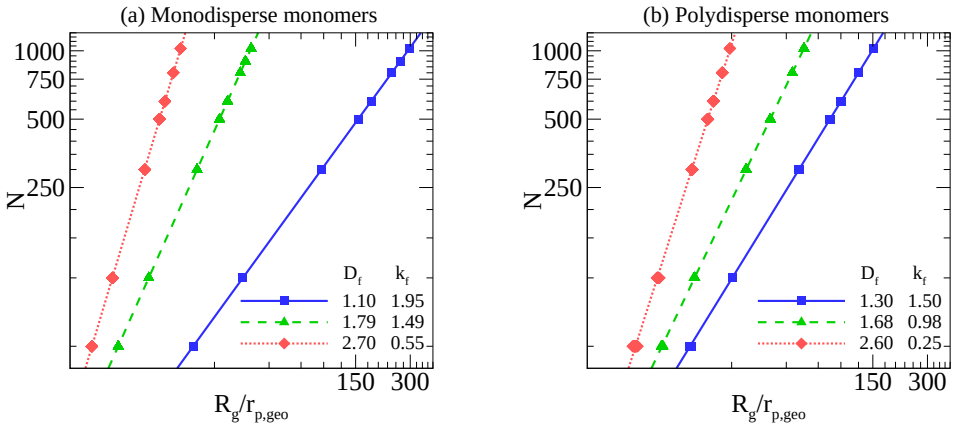

Figure 13: Preservation of fractal parameters for aggregates consisting of (a) monodisperse ($\sigma_{p,geo} = 1$) and (b) polydisperse ($\sigma_{p,geo} = 2$) primary particles for different combinations of fractal parameters (D_f and k_f). Continuous lines represent the log-log fit of the points, corresponding parameters are reported in the legend of the figures.

Once these aggregates are generated, numerical projections, like numerical TEM images [46], could be generated in order to relate the projected density-density correlation function as calculated by Nelson et al. [47] for numerically generated aggregates in comparison with experimentally measured ones. This feature will be available in a future version of FracVAL.[R1.C3]

5. Discussion

To demonstrate the advantage of FracVAL algorithm over the classical Filippov et al. [13] one, Fig. 14 compares the plots of $\log(N)$ as a function $\log(R_g/r_{p,geo})$ in log-log scale for aggregates generated using FracVAL and a direct application of the Filippov et al. [13][R1.C4] algorithm for polydisperse primary particles. The prescribed parameters are $D_f = 1.68$, $k_f = 0.98$, and $\sigma_{p,geo} = 2.0$ and for aggregate sizes from $N = 20$ to 1024. It is noticed that in the Filippov et al. [13] method considered Eq. (7) instead of the derived Eq. (6), which is used in FracVAL. Therefore, the effect of primary particle polydispersity on aggregate center of mass and radius of gyration

is not taken into account in the formulation of Filippov et al.. [13].[R1.C4] It is also worth pointing out that the FLAGE algorithm recently developed by Skorupski et al. [20] also made a direct application of the Filippov et al. [13][R1.C4] method for aggregates formed polydisperse primary particles and the results of Filippov et al. [13][R1.C4] shown in Fig. 14[R1.C4] should be identical to the results of FLAGE.

A total of 200 aggregates is generated using the method of Filippov et al. [13] for each set of parameters (D_f, k_f, N, and $\sigma_{p,geo}$). As can be seen, when primary particles are polydisperse, the classical Filippov et al. [13] does not preserve exactly the fractal parameters (D_f and k_f) for each individual aggregate, though the fractal parameters are preserved on an ensemble basis. Therefore, a large population of aggregates should be generated if one uses the Filippov et al. [13][R1.C4] method or the FLAGE code to generate aggregates formed by polydisperse primary particles. It is interesting to observe that the scatter of $\log(R_g/r_{p,geo})$ at a given N becomes increasingly smaller and the agreement between Filippov et al. [13] and FracVAL[R1.C5] is improved with increasing N. This agreement is employed in previous studies presented in the literature [46, 32].

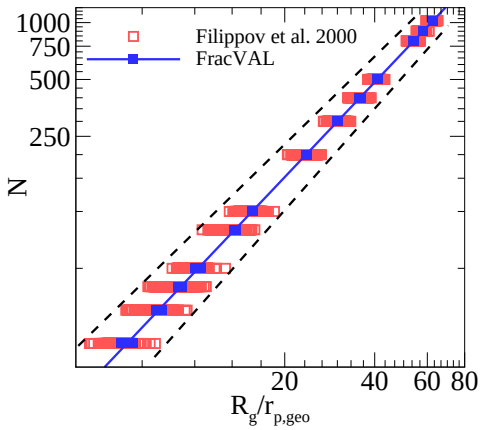

Figure 14: Comparison of results by using Filippov et al. [13] method and FracVAL. Aggregates consisting of $D_f = 1.68$ and $k_f = 0.98$ and $\sigma_{p,geo} = 2.0$.

Finally, the computational performance of the FracVAL algorithm is evaluated. The computations are carried out using a laptop equipped with a 2.40 GHz CPU and 8 Gb of memory. The reported CPU times are averaged over

a population of 100 aggregates for different combinations of D_f and k_f within the range of $D_f = 1.0 - 3.0$ and k_f between 0.1 and 2.4. The computational time is dependent on the number of monomers, the level of primary particle polydispersity, and the combination of D_f and k_f. Table 1 presents examples of average time required to generate an aggregate consisting of $N = 500$ for monomers polydispersity from $\sigma_{p,geo} = 1.0$ to 3.0. All examples of aggregates consisting of 500 PPs[R2.C4] are generated in less than 2.4 minutes. Meanwhile aggregates consisting of 1000 PPs are generated in less than 14 minutes. Generation of aggregates formed by polydisperse PPs is generally more time-consuming than those formed by monodisperse PPs.[R2.C4] It is important to remark that the majority of times is in the order of the minimum values reported in Table 1, while the maximum values are achieved only for combinations of extremely different D_f and k_f pairs and also these maximum times exhibit a much larger standard deviation than the minimum values.[R2.C4]

Table 1: Assessment of the average computational time (in seconds) required by FracVAL.

$\sigma_{p,geo}$	$N = 500$[R2.C4]	$N = 1000$[R2.C4]
1.00	1.1-70.1	5.3-84.6[R2.C4]
1.45	1.9-73.6	8.9-408[R2.C4]
2.00	3.9-145.8	28.2-791.1[R2.C4]
2.50	5.6-15.1	37.6-113.7-[R2.C4]
3.00	7.0-9.4	38-74.6[R2.C4]

6. Conclusions

A novel tunable cluster-cluster aggregation algorithm, FracVAL, is developed in this study to numerically generate fractal aggregates formed by polydisperse primary particles. The algorithm represents an improvement[R2.C4] of the tunable cluster-cluster aggregation algorithm of Filippov et al. [13] for generation of fractal aggregates formed by monodisperse primary particles. The algorithm is validated by comparing the density-density correlation functions of fractal aggregates generated by FracVAL and a literature method, FLAGE [20], and excellent agreement is observed. The prescribed fractal parameters D_f and k_f are found accurately preserved for each individual aggregate consisting of either monodisperse or polydisperse primary particles. The fractal properties of an ensemble of aggregates of different sizes are also

found to accurately preserve the prescribed D_f and k_f with less than 1% deviation for different combinations of D_f and k_f, regardless of the degree of primary particle polydispersity characterized by $\sigma_{p,geo}$ up to 3.

Since the positions of the two aggregating primary particles and the mass centers of the two aggregating clusters are found using analytical expressions by using the intersection of two spheres and random parameters, FracVAL is considerably computationally efficient for generating fractal aggregates for different combinations of D_f, k_f, and $\sigma_{p,geo}$ for $\sigma_{p,geo}$ up to 3, taking in average less than 2.4 minutes for $N = 500$ and 14 minutes for $N = 1000$ PPs[R2.C4] on a regular laptop, as long as the pair of D_f and k_f falls in the valid range where it is possible to generate such fractal aggregates.

Finally, it is demonstrated that the direct use of the tunable cluster-cluster aggregation algorithm Filippov et al. [13] to generate aggregates formed by polydisperse primary particles, such as implemented in the FLAGE code, does not preserve the prescribed fractal properties (D_f and k_f) for individual aggregates, though it does so globally, i.e., the fractal properties of an ensemble of aggregates recover the prescribed values. This observation suggests that caution should be taken when a certain property of individual aggregates formed by polydisperse primary particles generated by FLAGE is investigated, since the fractal dimension or prefactor may be different from the expected value. On the other hand, the algorithm developed in this study, FracVAL, overcomes the drawback of the Filippov et al. [13][R1.C4] method and the FLAGE code.

Acknowledgments

This work is supported by the Chilean CONICYT Research programs under Grant FONDECYT project 1161453 and partially by PIA-Anillo CyT project ACT172095.

References

[1] F. Babick, Suspensions of colloidal aggregates, in: Suspensions of Colloidal Particles and Aggregatess, Springer, 2016, pp. 119–220.
URL https://doi.org/10.1007/978-3-319-30663-6_4

[2] T. A. Witten, L. M. Sander, Phys. Rev. Lett. 47 (1981) 1400–1403. [link].
URL https://doi.org/10.1103/PhysRevLett.47.1400

[3] P. Meakin, Phys. Rev. Lett. 51 (1983) 1119–1122. [link].
URL https://doi.org/10.1103/PhysRevLett.51.1119

[4] M. Kolb, R. Botet, R. Jullien, Phys. Rev. Lett. 51 (1983) 1123–1126. [link].
URL https://doi.org/10.1103/PhysRevLett.51.1123

[5] R. C. Ball, T. A. Witten, Phys. Rev. A 29 (1984) 2966–2967. [link].
URL https://doi.org/10.1103/PhysRevA.29.2966

[6] S. Tolman, P. Meakin, Phys. Rev. A 40 (1989) 428–437. [link].
URL https://doi.org/10.1103/PhysRevA.40.428

[7] P. Meakin, J. Sol-Gel Sci. Technol. 15 (2) (1999) 97–117. [link].
URL https://doi.org/10.1023/A:1008731904082

[8] F. Braga, M. S. Ribeiro, Comput. Phys. Commun. 182 (8) (2011) 1602 – 1605. [link].
URL https://doi.org/10.1016/j.cpc.2011.04.005

[9] K. R. Kuijpers, L. de Martín, J. R. van Ommen, Comput. Phys. Commun. 185 (3) (2014) 841–846. [link].
URL https://doi.org/10.1016/j.cpc.2013.12.003

[10] C. Li, H. Xiong, Comput. Phys. Commun. 185 (12) (2014) 3424–3429. [link].
URL https://doi.org/10.1016/j.cpc.2014.08.017

[11] R. Thouy, R. Jullien, J. Phys. A: Math. Gen. 27 (9) (1994) 2953–2963. [link].
URL https://doi.org/10.1088/0305-4470/27/9/012

[12] D. W. Mackowski, Appl. Opt. 34 (18) (1995) 3535–45. [link].
URL https://doi.org/10.1364/AO.34.003535

[13] A. Filippov, M. Zurita, D. Rosner, J. Colloid Interface Sci. 229 (1) (2000) 261–273. [link].
URL https://doi.org/10.1006/jcis.2000.7027

[14] U. Kätzel, R. Bedrich, M. Stintz, R. Ketzmerick, T. Gottschalk-Gaudig, H. Barthel, Part. Part. Syst. Char. 25 (1) (2008) 9–18. [link].
URL https://doi.org/10.1002/ppsc.200700004

[15] R. K. Chakrabarty, M. A. Garro, S. Chancellor, C. Herald, H. Moosmüller, Comput. Phys. Commun. 180 (8) (2009) 1376–1381. doi:https://doi.org/10.1016/j.cpc.2009.01.026.

[16] C. Ringl, H. M. Urbassek, Comput. Phys. Commun. 184 (7) (2013) 1683–1685. [link].
URL https://doi.org/10.1016/j.cpc.2013.02.012

[17] L. Ehrl, M. Soos, M. Lattuada, J. Phys. Chem. B 113 (31) (2009) 10587–10599. [link].
URL https://doi.org/10.1021/jp903557m

[18] S. Prasanna, P. Rivière, A. Soufiani, J. Quant. Spectrosc. Radiat. Transfer 148 (2014) 141 – 155. [link].
URL https://doi.org/10.1016/j.jqsrt.2014.07.004

[19] A. D. Melas, L. Isella, A. G. Konstandopoulos, Y. Drossinos, J. Colloid Interface Sci. 417 (2014) 27 – 36. [link].
URL https://doi.org/10.1016/j.jcis.2013.11.024

[20] K. Skorupski, J. Mroczka, T. Wriedt, N. Riefler, Physica A 404 (2014) 106–117. [link].
URL https://doi.org/10.1016/j.physa.2014.02.072

[21] M. L. Eggersdorfer, S. E. Pratsinis, Aerosol Sci. Technol. 46 (3) (2012) 347–353. [link].
URL https://doi.org/10.1080/02786826.2011.631956

[22] R. Dastanpour, S. N. Rogak, J. Aerosol Sci. 94 (2016) 22–32. [link].
URL https://doi.org/10.1016/j.jaerosci.2015.12.005

[23] M. Tence, J. P. Chevalier, R. Jullien, J. Physique 47 (11) (1986) 1989–1998. [link].
URL https://doi.org/10.1051/jphys:0198600470110198900

[24] G. Bushell, R. Amal, J. Colloid Interface Sci. 205 (2) (1998) 459–469. [link].
URL https://doi.org/10.1006/jcis.1998.5667

[25] G. Bushell, R. Amal, J. Raper, Part. Part. Syst. Char. 15 (1998) 3–8. [link].
URL https://doi.org/10.1002/(SICI)1521-4117(199802)15:1<3::AID-PPSC3>3.0.CO;2-

[26] T. L. Farias, Ü. Ö. Köylü, M. G. Carvalho, J. Quant. Spectrosc. Radiat. Transfer 55 (3) (1995) 357–371. [link].
URL https://doi.org/10.1016/0022-4073(95)00166-2

[27] T. Seto, A. Hirota, T. Fujimoto, M. Shimada, K. Okuyama, Aerosol Sci. Technol. 27 (3) (1997) 422–438. [link].
URL https://doi.org/10.1080/02786829708965482

[28] T. T. Charalampopoulos, G. Shu, Appl. Opt. 41 (4) (2002) 723–733. [link].
URL https://doi.org/10.1364/AO.41.000723

[29] F. Liu, M. Yang, F. Hill, D. Snelling, G. Smallwood, Appl. Phys. B 83 (3) (2006) 383. [link].
URL https://doi.org/10.1007/s00340-006-2196-z

[30] M. C. Heine, S. E. Pratsinis, J. Aerosol Sci. 38 (1) (2007) 17–38. [link].
URL https://doi.org/10.1016/j.jaerosci.2006.09.005

[31] J. Y. Yin, L. H. Liu, J. Quant. Spectrosc. Radiat. Transfer 111 (14) (2010) 2115–2126. [link].
URL https://doi.org/10.1016/j.jqsrt.2010.05.016

[32] C. Liu, Y. Yin, F. Hu, H. Jin, C. M. Sorensen, Aerosol Sci. Technol. 49 (10) (2015) 928–940. [link].
URL https://doi.org/10.1080/02786826.2015.1085953

[33] E. Goudeli, M. L. Eggersdorfer, S. E. Pratsinis, Langmuir 32 (36) (2016) 9276–9285. [link].
URL https://doi.org/10.1021/acs.langmuir.6b02455

[34] J. Yon, F. Liu, J. Morán, A. Fuentes, Proc. Combust. Inst.[link].
URL https://doi.org/10.1016/j.proci.2018.07.065

[35] A. Spyrogianni, K. S. Karadima, E. Goudeli, V. G. Mavrantzas, S. E. Pratsinis, J. Chem. Phys. 148 (6) (2018) 064703. [link].
URL https://doi.org/10.1063/1.5012037

[36] A. Bescond, J. Yon, F. X. Ouf, D. Ferry, D. Delhaye, D. Gaffié, A. Coppalle, C. Rozé, Aerosol Sci. Technol. 48 (8) (2014) 831–841. [link].
URL https://doi.org/10.1080/02786826.2014.932896

[37] D. Boldridge, Aerosol Sci. Technol. 44 (3) (2010) 182–186. [link].
URL https://doi.org/10.1080/02786820903499462

[38] S. Bau, O. Witschger, F. Gensdarmes, O. Rastoix, D. Thomas, Powder Technol. 200 (3) (2010) 190–201. [link].
URL https://doi.org/10.1016/j.powtec.2010.02.023

[39] D. Cortés, J. Morán, F. Liu, F. Escudero, J.-L. Consalvi, A. Fuentes, Energy Fuels 32 (11) (2018) 11802–11813. [link].
URL https://doi.org/10.1021/acs.energyfuels.8b01301

[40] C. M. Sorensen, G. D. Feke, Aerosol Sci. Technol. 25 (3) (1996) 328–337. [link].
URL https://doi.org/10.1080/02786829608965399

[41] C. Forbes, M. Evans, N. Hastings, B. Peacock, Statistical distributions, John Wiley & Sons, 2011.

[42] C. M. Sorensen, C. Oh, Phys. Rev. E 58 (1998) 7545–7548. [link].
URL https://doi.org/10.1103/PhysRevE.58.7545

[43] J. S. Dai, Mech. Mach. Theory 92 (2015) 144–152. [link].
URL https://doi.org/10.1016/j.mechmachtheory.2015.03.004

[44] R. Jullien, Contemp. Phys. 28 (5) (1987) 477–493. [link].
URL https://doi.org/10.1080/00107518708213736

[45] A. Hasmy, M. Foret, J. Pelous, R. Jullien, Phys. Rev. B 48 (13) (1993) 9345. [link].
URL https://doi.org/10.1103/PhysRevB.48.9345

[46] J. Morán, J. Cuevas, F. Liu, J. Yon, A. Fuentes, Powder Technol. 330 (2018) 67 – 79. [link].
URL https://doi.org/10.1016/j.powtec.2018.02.008

[47] J. A. Nelson, R. J. Crookes, S. Simons, J. Phys. D 23 (4) (1990) 465. [link].
URL http://stacks.iop.org/0022-3727/23/i=4/a=014

Appendix A. Derivation of Eq.(6)

The resulting center of mass (R_c) of an aggregate formed by the aggregation of two clusters of N_1 and N_2 PPs with mass m_1 and m_2, respectively is,

$$mR_c = \sum_{i=1}^{N} m_{p,i} R_i = \sum_{j=1}^{N_1} m_{p,j} R_j + \sum_{k=1}^{N_2} m_{p,k} R_k, \tag{A.1}$$

where $N_1 + N_2 = N$ and $m_1 + m_2 = m$. Therefore,

$$mR_c = m_1 R_{c1} + m_2 R_{c2}. \tag{A.2}$$

Let's Γ be the vector that stands for the distance between the center of mass of the two sub-clusters,

$$\Gamma = R_{c2} - R_{c1}, \tag{A.3}$$

getting m_1 and m_2 from the relation $m = m_1 + m_2$ and replacing their values in Eq. (A.2) we can obtain,

$$R_{c1} - R_c = -\frac{m_2}{m}\Gamma, \tag{A.4a}$$

$$R_{c2} - R_c = \frac{m_1}{m}\Gamma, \tag{A.4b}$$

On the other hand, from the radius of gyration of the original aggregate calculated from Eq. (4) we obtain,

$$\begin{aligned} m^2 R_g^2 \;=\; & \textstyle\sum_{j=1}^{N_1} m_{p,j} \left[(R_j - R_{c1} + R_{c1} - R_c)^2 + r_{g,p,j}^2 \right] + \\ & \textstyle\sum_{k=1}^{N_2} m_{p,k} \left[(R_k - R_{c2} + R_{c2} - R_c)^2 + r_{g,p,k}^2 \right], \end{aligned} \tag{A.5}$$

$$\begin{aligned} m^2 R_g^2 \;=\; & \textstyle\sum_{j=1}^{N_1} m_{p,j} \left[(R_j - R_{c1})^2 + r_{g,p,j}^2 + \right. \\ & \left. 2(R_j - R_{c1})(R_{c1} - R_c) \right] + \\ & \textstyle\sum_{k=1}^{N_2} m_{p,k} \left[(R_k - R_{c2})^2 + r_{g,p,k}^2 + \right. \\ & \left. 2(R_k - R_{c2})(R_{c2} - R_c) \right] + \\ & m_1 (R_{c1} - R_c)^2 + m_2 (R_{c2} - R_c)^2, \end{aligned} \tag{A.6}$$

where the terms: $\sum_{j=1}^{N_1} 2m_{p,j}(R_j - R_{c1})(R_{c1} - R_c)$ and $\sum_{k=1}^{N_2} 2m_{p,k}(R_k - R_{c2})(R_{c2} - R_c)$ are both equal to zero.

$$m^2 R_g^2 = \begin{array}{l} \sum_{j=1}^{N_1} m_{p,j} \left[(R_j - R_{c1})^2 + r_{g,p,j}^2 \right] + m_1 (R_{c1} - R_c)^2 + \\ \sum_{k=1}^{N_2} m_{p,k} \left[(R_k - R_{c2})^2 + r_{g,p,k}^2 \right] + m_2 (R_{c2} - R_c)^2, \end{array} \tag{A.7}$$

combining this result with Eq. (A.4a) and Eq. (A.4b) and introducing R_{g1} and R_{g2} as the radius of gyration of both sub-clusters we get,

$$m^2 R_g^2 = m \left(m_1 R_{g1}^2 + m_2 R_{g2}^2 \right) + \Gamma^2 m_1 m_2, \tag{A.8}$$

if we consider the particular case of aggregates consisting of monodisperse PPs with mass m_p, consequently $m = N m_p$, $m_1 = N_1 m_p$ and $m_2 = N_2 m_p$, then Eq. (6) turns to,

$$N^2 R_g^2 = N \left(N_1 R_{g1}^2 + N_2 R_{g2}^2 \right) + \Gamma^2 N_1 N_2, \tag{A.9}$$

which is equivalent to the relationship derived by Filippov et al. [13].

Appendix B. Sphere-sphere intersection

Lets consider two spheres in $\Re^3$ with equations,

$$(x - x_1)^2 + (y - y_1)^2 + (z - z_1)^2 = r_1^2, \tag{B.1a}$$

$$(x - x_2)^2 + (y - y_2)^2 + (z - z_2)^2 = r_2^2. \tag{B.1b}$$

Lets d be the distance between the center of the two spheres. Based in the law of cosines,

$$\cos[\alpha] = \frac{-r_2^2 + r_1^2 + d^2}{2 r_1 d}, \tag{B.2}$$

The intersection of these two spheres is a circle contained in the plane of intersection. Lets ρ be the radius of this circle, then $\rho = r_1 \sin[\alpha]$, considering Eq. (B.2) and the identity $\sin^2[\alpha] + \cos^2[\alpha] = 1$ we obtain,

$$\rho = \frac{1}{2d} \sqrt{4 r_1^2 d^2 - \left(-r_2^2 + r_1^2 + d^2 \right)^2}. \tag{B.3}$$

On the other hand, the plane of intersection is obtained by subtracting Eq. (B.1a) and Eq. (B.1b) by considering $A = 2(x_2 - x_1)$, $B = 2(y_2 - y_1)$, $C = 2(z_2 - z_1)$ and $D = (r_1^2 - r_2^2) + (x_2^2 - x_1^2) + (y_2^2 - y_1^2) + (z_2^2 - z_1^2)$,

$$Ax + By + Cz = D. \tag{B.4}$$

641 The equation of the line that connect the centers of the two spheres is,

$$x = x_1 + t(x_2 - x_1), \quad y = y_1 + t(y_2 - y_1), \quad z = z_1 + t(z_2 - z_1), \tag{B.5}$$

642 The intersection of this line and the plane given by Eq. (B.4) bring us
643 the value of the constant t as following,

$$t = \frac{Ax_1 + By_1 + Cz_1 - D}{A(x_1 - x_2) + B(y_1 - y_2) + C(z_1 - z_2)}, \tag{B.6}$$

644 replacing in Eq. (B.5) we obtain the coordinates $\vec{c}$ of the center of the
645 circle of intersection between the two spheres. Finally, with the coordinates
646 of the center $\vec{c}$ and the radius ρ, the equation of the circle of intersection of
647 the two spheres can be parametrized as follows,

$$\vec{r}[\psi] = \vec{c} + \rho\cos[\psi]\hat{i}' + \rho\sin[\psi]\hat{j}', \qquad \psi \in [0, 2\pi] \tag{B.7}$$

648 where $\hat{i}'$ and $\hat{j}'$ are two perpendicular unit vectors belonging to the plane
649 given by Eq. (B.4).

650 Appendix C. Sensitivity analysis to initial sub-clusters morphol-
651 ogy and size

652 We intend to answer the following question: how important are the ini-
653 tial sub-clusters to the final aggregates generated with FracVAL? To this end
654 a sensitivity analysis of the density pair-correlation function $f(r)$ is carried
655 out. For aggregates consisting of $N = 100$ monomers a sensitivity analysis
656 is developed for monodisperse (Fig. C.15(a) and Fig. C.15(b)) and poly-
657 disperse (Fig. C.15(c) and Fig. C.15(d)) primary particles. A total of 3
658 parameters are varied. In Fig. C.15(a) and Fig. C.15(c) the sensitivity of
659 the density pair-correlation function $f(r)$ to the size of initial sub-clusters is
660 tested considering $N_{sub} = 5$, 10 and 15% (expressed in a percentage of N).
661 The other two parameters considered are the fractal dimension and prefactor
662 used for the generation of sub-clusters. The sensitivity of the density pair-
663 correlation function $f(r)$ to D_f and k_f with a variation of $\pm$ 20% is reported
664 in Fig. C.15(b) and Fig. C.15(d) for monodisperse and polydisperse PPs,

respectively. Please note that in the latter cases only the fractal parameters of the sub-clusters are variated meanwhile those corresponding to the final aggregate remain constant (fixed to the original imposed D_f and k_f). As expected, for all cases consisting of monodisperse PPs there is no variation for $r/r_{p,geo} \leq 2$, because at this scale only intersection between equally sized spheres is found. For larger ranges $r/r_{p,geo} > 2$ the overall behaviour of the pair correlation function is not significantly affected by the three concerned parameters except in the polydisperse PPs case when the fractal dimension of the sub-cluster is strongly modified ($\pm$ 20%). Nevertheless, the effect seems limited to the domain of $r/r_{p,geo} \in [2, 8]$.

Appendix D. Further explanation of cases 2 and 3 of section 3.2

In the context of Section 3.2 in sub-step 4b we identified 3 possible cases of aggregation of two sub-clusters A1 and A2. The main part of the manuscript is devoted to explain Case 1 for being considered as the most common case. This appendix intends to provide a detailed explanation of Cases 2 and 3.

- Case 2: When the sphere of radius $D_{i1,+}$ is large to enclose the sphere of radius $D_{j2,+}$, i.e., when $(D_{i1,+} - D_{j2,+}) > \Gamma_{12}$ with an upper limit $D_{i1,-} \leq \Gamma_{12} + D_{j2,+}$. Please see Fig. D.16.

- Case 3: Analogously, when the sphere of radius $D_{j2,+}$ is large to enclose the sphere of radius $D_{i1,+}$, i.e., when $(D_{j2,+} - D_{i1,+}) > \Gamma_{12}$ with an upper limit $D_{j2,-} \leq \Gamma_{12} + D_{i1,+}$.

In the context of sub-step 4c, there are three different scenarios for joining the sub-cluster A1 and A2 by selecting the candidate primary particles s1 (belonging to A1) and s2 (belonging to A2). Therefore, we will be concerned about the following spheres,

$$Sph.1: \; D^2_{s1,+} = (X - X_{cm,1})^2 + (Y - Y_{cm,1})^2 + (Z - Z_{cm,1})^2, \tag{D.1a}$$

$$Sph.2: \; D^2_{s1,-} = (X - X_{cm,1})^2 + (Y - Y_{cm,1})^2 + (Z - Z_{cm,1})^2, \tag{D.1b}$$

$$Sph.3: \; D^2_{s2,+} = (X - X_{cm,2})^2 + (Y - Y_{cm,2})^2 + (Z - Z_{cm,2})^2, \tag{D.1c}$$

$$Sph.4: \; D^2_{s2,-} = (X - X_{cm,2})^2 + (Y - Y_{cm,2})^2 + (Z - Z_{cm,2})^2. \tag{D.1d}$$

The reason that many spheres appear is that the possible solutions, i.e., the intersections between s1 and s2, correspond to the intersection of two

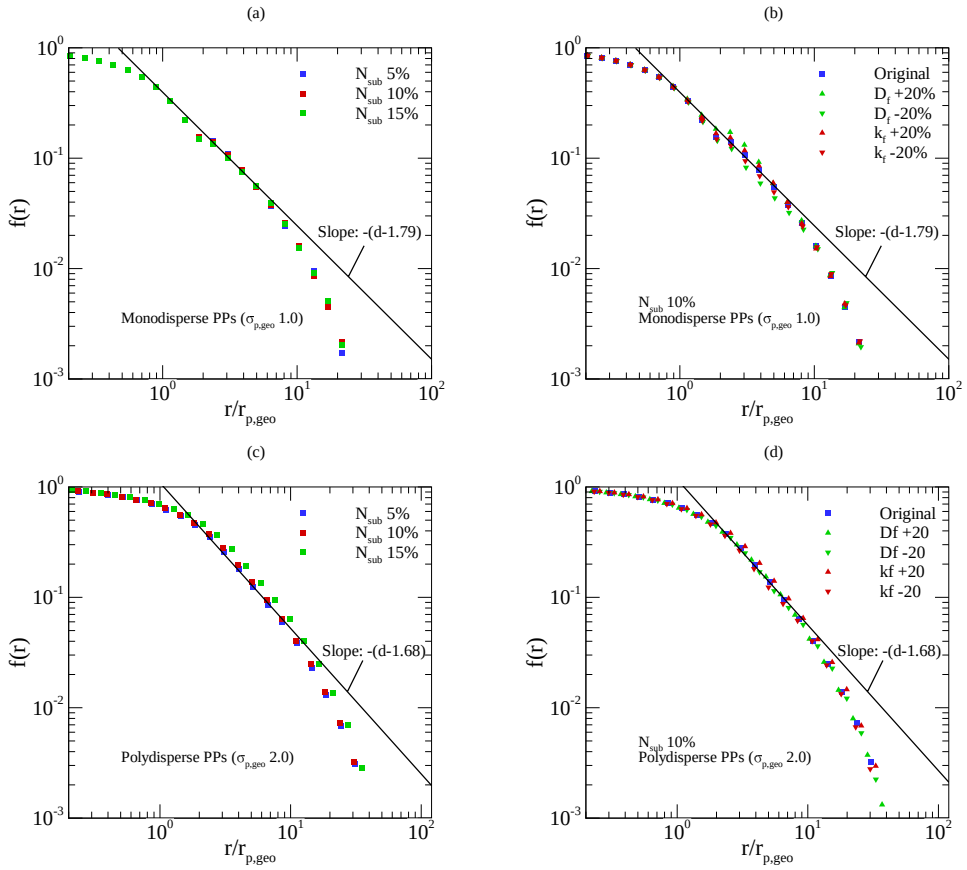

Figure C.15: Sensitivity analysis of density-density correlation function for the initial sub-clusters consisting of monodisperse (a and b) and polydisperse PPs (Figs. c and d). Figs. (a) and (c) illustrate the sensitivity of the initial sub-clusters size (N_{sub}), and Figures (b) and (d) show the sensitivity to fractal parameters (D_f and k_f). All aggregates consist of $N = 100$ monomers, fractal parameters $D_f = 1.79$ and $k_f = 1.40$ for monodisperse ($\sigma_{p,geo} = 1$) and $D_f = 1.68$ and $k_f = 0.98$ for polydisperse PPs ($\sigma_{p,geo} = 2$).

spherical shells. The spherical shell belonging to A1 is determined by the concentric spheres Sph.1 and Sph.2 and the spherical shell belonging to A2 is analogously determined by the spheres Sph.3 and Sph.4. The above mentioned 3 possible scenarios are described as follows,

- Please note that the intersection of spheres 2 and 4 is not possible and therefore it does not lead to any possible solution.
- Scenario 1: When $\Gamma_{12} \geq |D_{s1,+} - D_{s2,+}|$. In this case (considered

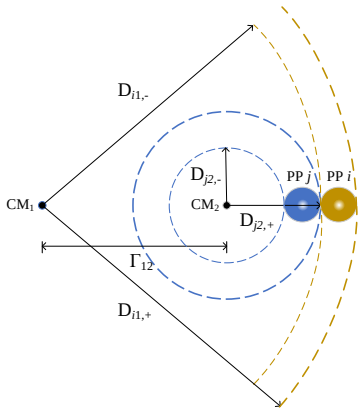

Figure D.16: Limiting candidate for Case 2 ($D_{i1,+}$ is large to enclose the sphere of radius $D_{j2,+}$). This is analogous to Case 3.

the most common) we examine a random point in the spherical cap belonging to Sph.1 generated by the intersection of spheres Sph.1 and Sph.3 as illustrated in Fig. D.17(a). Once this point is selected, the position of monomer s1 is finally set by a displacement of the radius of monomer s1 (r_{s1}) in the unitary direction defined by CM1 and the current position of s1 (vector pointing to s1). Additionally, the spheres Sph.1 and Sph.4 can also intersect. In this case, the solution is found in the spherical segment illustrated in Fig. D.17(b).

Any point in the spherical cap (Fig. D.17(a)) or spherical segment (Fig. D.17(b)) can be a solution for finding a point contact between s1 and s2; however, this process of search may be very time consuming. That is the reason why FracVAL offers the option of enabling or disabling (by a binary value in the code) the search of random points on these surfaces. The other option is simply to select the intersection between the two larger spheres as described in section 3.2.

- Scenario 2: When $\Gamma_{12} < D_{s1,+} - D_{s2,+}$ and $\Gamma_{12} > D_{s1,-} - D_{s2,+}$. In this case, we search a random point in the spherical cap belonging to Sph.2 generated by the intersection of Sph.2 and Sph.3. Once this point is selected the position of s1 is finally set by a displacement of r_{s1} in the unitary direction defined by CM1 and the current position of s1 (vector pointing to s1). Please refer to the illustration of Fig. D.18(a), as can

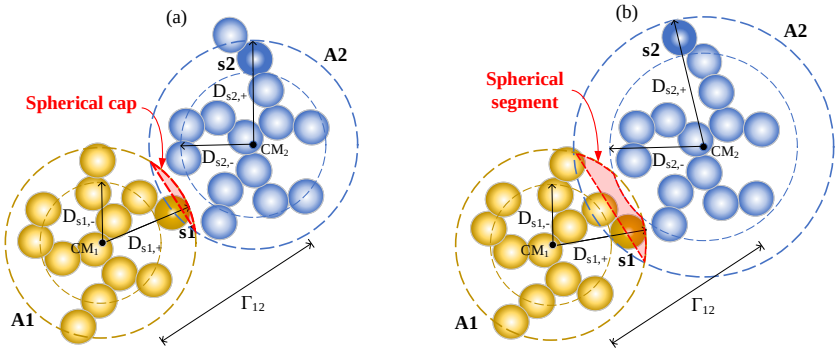

Figure D.17: (a) Spherical cap corresponding to A1, given by the intersection of Sph.1 and Sph.3. (b) Truncated spherical cap or spherical segment corresponding to A1, given by the intersection of Sph.1 and Sph.3 and limited by Sph.4.

be seen, the solution of Scenario 1 is not possible because sphere Sph.1 (radius $D_{s1,+}$) is too big and therefore there is no intersection with sphere Sph.3 (radius $D_{s2,+}$). In this case, the position of monomer s1 is found in the spherical cap of sphere Sph.2 (radius $D_{s1,-}$) generated by the intersection of spheres Sph.2 and Sph.3.

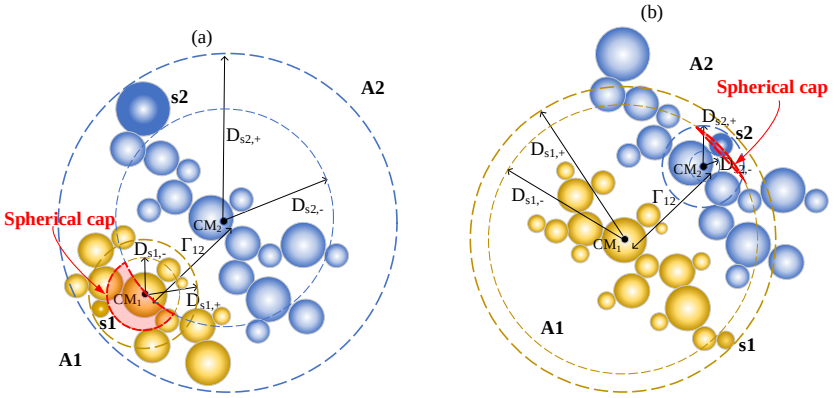

Figure D.18: (a) Example of scenario 2. (b) Example of scenario 3.

- Scenario 3: When $\Gamma_{12} < D_{s2,+} - D_{s1,+}$ and $\Gamma_{12} > D_{s2,-} - D_{s1,+}$. In this case, we examine a random point in the spherical cap belonging

to Sph.2 generated by the intersection of Sph.2 and Sph.4. Once this point is selected the position of s1 is finally set by a displacement of r_{s1} in the opposite unitary direction defined by CM1 and the current position of s1 (vector pointing to s1). The solution of Scenario 1 is not possible because sphere Sph.3 (of radius $D_{s2,+}$) is large and therefore there is no intersection with sphere Sph.1 (of radius $D_{s1,+}$). In this case, the position of monomer s1 is found in the spherical cap of sphere Sph.2 (of radius $D_{s1,-}$) generated by the intersection of spheres Sph.2 and Sph.4 (please refer to Fig. D.18(b) for more details).